ABSTRACT

Title of Thesis: DEVELOPMENTS IN CARBON FIBER ROD ANALYSIS FOR SPORTING GOODS APPLICATIONS

Connor Robert Quigley
Master of Science, 2022

Thesis Directed By: Professor Peter W. Chung
Department of Mechanical Engineering

In sporting goods manufacturing, such as in fishing rod design, new products are created using an Edisonian process. By changing the geometry of the carbon fiber prepreg layup, a rod can be constructed that lends itself to a specific application. This thesis will present an integrated computational materials engineering (ICME) approach for carbon fiber fishing rods using simulation theory and experiments. The computations are based on the finite element method (FEM), including the use of integrated Euler-Bernoulli beam theory in MATLAB. The experimental methodology uses three-point bending (3PB) flexure test analysis to determine values for Young's Modulus which are then incorporated into numerical solutions and modelling. Discretized values for Young's Modulus are used in thin-walled tapered cylindrical Euler-Bernoulli beam models through variable second area moment of inertia (I_y) and constant I_y approaches. The 3PB flexural experiments performed on a test rod section agree to FEM solutions, along with convergence with respect to mesh size between variable I_y and constant I_y beam models. A modal analysis on the beam provides insight to the free-vibrational effects of a fishing rod under differing boundary conditions. Through this ICME approach, rod manufacturers can understand properties in rod prototypes and better develop future rod models.

DEVELOPMENTS IN CARBON FIBER ROD ANALYSIS FOR SPORTING GOODS APPLICATIONS

By

Connor Robert Quigley

Thesis submitted to the Faculty of the Graduate School of the
University of Maryland, College Park in partial fulfillment
of the requirements of the degree of
Master of Science
2022

Advisory Committee:
Professor Peter Chung, Chair/Advisor
Professor Abhijit Dasgupta
Professor Jeffery Herrmann

Acknowledgements

My very first and foremost gratitude goes to my advisor, Prof. Peter Chung for his consistent enlightenment, patience, and guidance throughout this entire process of studying and researching. His unparalleled knowledge and kindness are what made this project possible. I would also like to thank Prof. Dasgupta and Prof. Herrmann for their advice and support as my committee members.

I would like to thank Thomas and Thomas in Greenfield MA for their industry insights and test specimens provided for this work.

Special thanks to my friends and peers throughout my journey at the University of Maryland. With their constant friendship and support, they made this chapter of my life truly special.

Finally, I would like to thank my parents for their unconditional love and support for me and my dreams.

Table of Contents

List of Figures

List of Tables

Chapter 1: Introduction

1.1 Motivation

With the ability to form many geometries, carbon fiber lends itself to many applications. One of the most useful forms of carbon fiber is carbon fiber prepreg. Prepreg in this case is short for pre-impregnated. In this form, unidirectional carbon fiber filaments are manufactured with a pre-impregnated resin and supporting scrim layer to help with manufacturing processing. This carbon fiber prepreg has longitudinal, transverse, and normal properties with respect to the unidirectional (longitudinal) fiber direction (Figure 1).

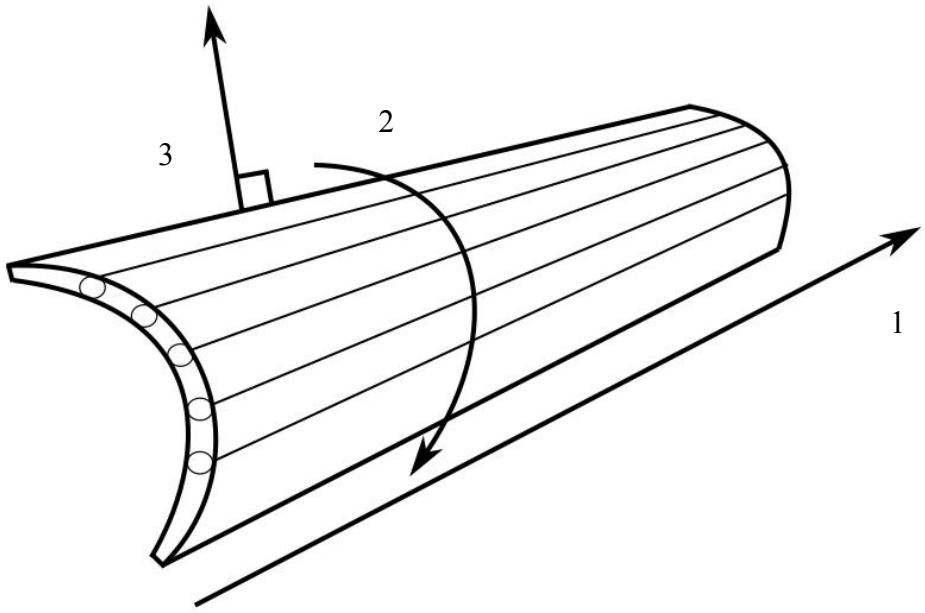

Figure 1 – Unidirectional prepreg with unique longitudinal (1), transverse (2), and normal (3) properties.

The resin, when heated to a specific temperature, will impregnate the carbon fiber filaments and bond the filaments to adhere to the geometry of the desired part. The scrim layer helps in the transportation and storage of the prepreg roll, as without this differing ply scrim, the prepreg would be fragile and the carbon filaments could become damaged easily.

The developments in carbon fiber prepreg production in the latter half of the 1900s gave way to the material being used for many new applications. Aside from aerospace and industrial applications, the prepreg was also adapted to be used by sporting goods manufactures. By rolling the prepreg around a mandrel, a rod can be made with properties that excel the fiberglass and natural materials common in the past. In this case, the use of carbon fiber in fishing rods will be examined and studied.

1.2 History and Rationale

Before the use of carbon fiber, rods were primarily constructed of bamboo or fiberglass. Fiberglass does not have the best stiffness for its size and weight, and rods constructed with fiberglass tended to be very heavy, even more so than their bamboo counterparts [1].

When carbon fiber rod manufacturing became standardized in the 1970's, major rod manufactures jumped on this new 'space age' material. Lighter, stiffer, and greater damping response of the carbon fiber yielded to a plethora of new rod designs and applications [1].

When the rod is held in the hand for long periods of fishing, as in fly fishing, the weight of the rod can affect the angler's experience. The rod's mass moment of inertia that is felt in the wrist and hand, known in fly fishing as "swing weight," was greatly reduced and allowed for more power and energy to be transmitted to the line during the casting stroke [2].

These advancements in rod manufacturing technology superseded the analytical procedures of the time. With the modern advancements in experimental design and computer simulations, the goal of this thesis is to quantify the properties of a carbon fiber rod to better understand the ways that manufacturing can be streamlined and analyzed. To this day, many rods are manufactured by hand, and the design of new rods is done with an Edisonian 'guess and check' process. This thesis serves as the groundwork to better understand the intrinsic properties of a carbon fiber rod, and how manufactures can use an ICME approach to accelerate the design process and create the best possible product.

1.3 Manufacturing

The carbon fiber arrives at the rod factory in a sheet called prepreg. This sheet has pre-impregnated fibers that have an uncured matrix material. This sheet is cut into smaller 'flags' and rolled (Figure 2) around the tapered steel mandrel coated with a wax removal agent.

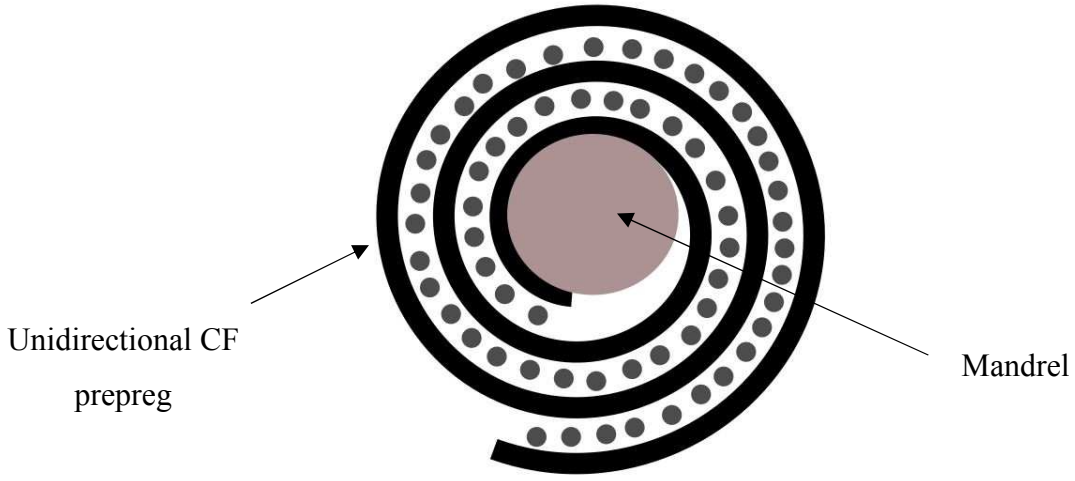

Figure 2 – Prepreg around mandrel

The tip section of a fly rod is very thin, and may only have a few plies (layers), whereas the butt section (handle end) has many more plies. When the prepreg is applied to the mandrel, the side of the prepreg that is tacked down has its unidirectional fibers parallel to the length of

the mandrel (Figure 3). This "flag" of prepreg material is not a rectangular sheet. The flag is cut from a sheet of unidirectional prepreg that has been determined to provide a consistent amount of material around the circumference of the mandrel.

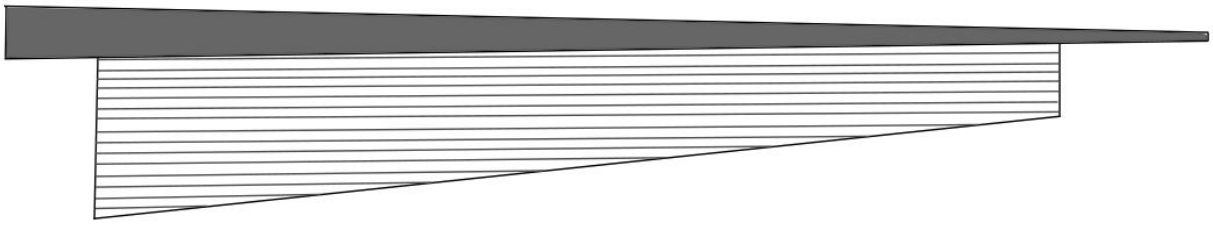

Figure 3 – Prepreg tacked to mandrel

It is important to note that after rolling the tapered mandrel with the prepreg material attached the fibers during each consecutive wrap will not adhere to a uniaxial direction as shown in Figure 4.

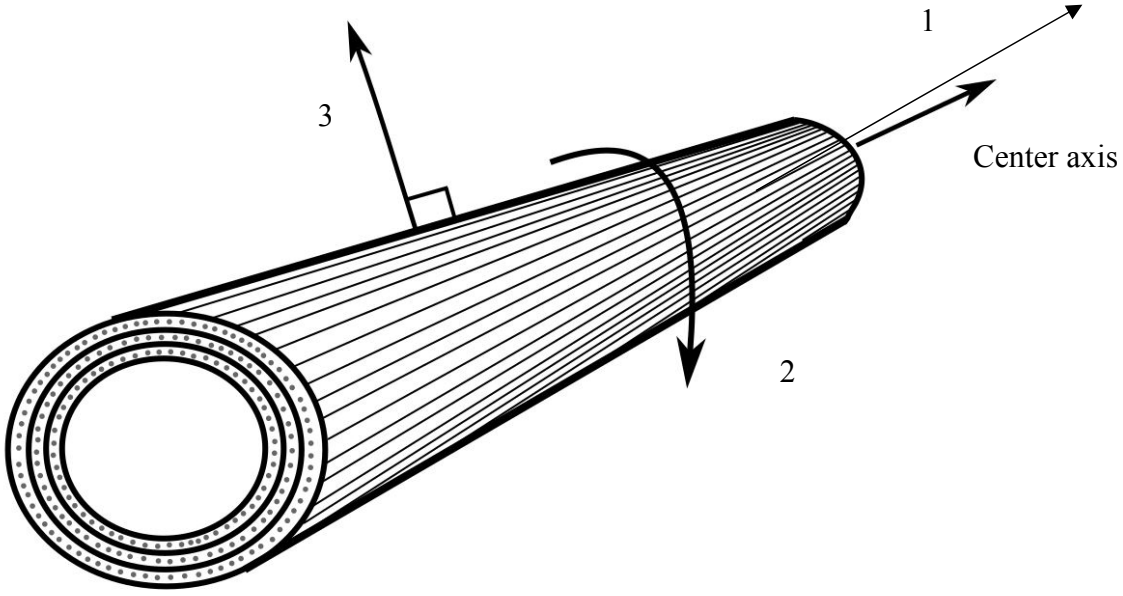

Figure 4 – Direction of Unidirectional Carbon fibers after rolling. The directions of longitudinal (1) and transverse (2) will not align with center axis after the prepreg is rolled around the tapered mandrel.

The prepreg resin is extremely important in the rod design. The resin not only acts as a bonding agent for the plies, but it also protects the carbon fiber structure. Many companies today use small particles in the resin to fill in extremely small gaps in the carbon fiber matrix [3].

Once the rod is wrapped around the mandrel, it is tightly wrapped in a cellophane tape that pushes the layered carbon tightly together around the mandrel. This cellophane tape also shrinks during the curing process, and reduces gaps between the prepreg and mandrel. The uncured resin now must be activated via the curing process. The rods are put into a large curing oven where they go through a cycle of specific temperatures. The rods are brought up from room temperature and held at time specific temperature plateaus that match the resin manufacturer's specifications. After cooling, the mandrel is pneumatically removed from the cured rod and the cellophane tape is removed. Any error in this process can result in an undetectable failure mode of the blank [4].

1.4 Research Methods

The development of an Integrated Computational Materials Engineering (ICME) approach to studying the thin-walled tapered beam is beneficial to understanding the bending characteristics of fishing rods. Deflection curves are commonly used in the fishing rod industry to understand the taper and bending characteristics of a certain rod profile and design. Rods have many different "action" profiles, which can consist of fast, progressive, and slow, as commonly used in the industry [2]. When the rod is loaded, as in during a cast, the rod will exhibit different flexure qualities depending on the taper and material used in the rod (Figure 5). For example, rods made with fiberglass with a lower modulus than carbon fiber will exhibit a

slower action. Rods of similar length and stiffness can be compared from manufacturer to manufacturer (Figure 6).

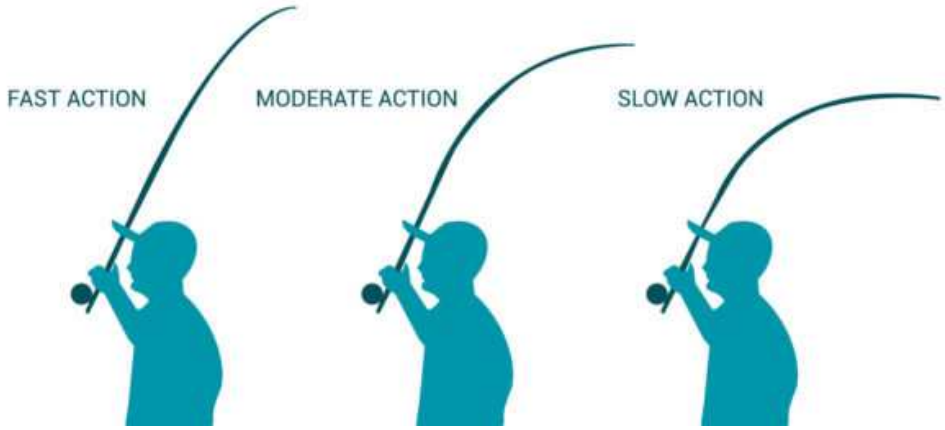

Figure 5 – Fly Rod Actions [5]

Figure 6 – Fly rod deflection curves [6]

A previous isotropic beam model was developed in ANSYS to determine the flexure characteristics of a rod, but this yielded low accuracy and adherence to the experiments performed. By using a linear isotropic beam, the rod needed to be discretized into constant diameter sections for the calculation [7]. This model also did not consider the variation in

Young's Modulus. A tapered beam model was developed that allowed for higher accuracy compared to experiments. This justifies the use of a tapered second area moment of inertia as used in the calculations [8].

1.5 Research Goals and Objectives

By developing an approach that studies the rod as a beam, the effects of complex geometry and carbon prepreg layups can be accounted for in the variation in the second area moment of inertia and the variation in Young's Modulus over the length of the beam. Flexure tests can be performed, along with modal analysis in order to determine the flexure profiles and mode shapes of a rod. These mode shapes can be used to help understand and achieve controlled rebound of the rod to a steady state position after a cast is performed. By considering the variation in young's modulus and area moment of inertia, a rod designer can balance these attributes to gain insight into the mechanical properties of fishing rods in order to aid the design process.

Chapter 2: Methods

2.1 Assumptions and Approximations

Euler – Bernoulli (EB) beam theory was used in this work. This introduced all the standard assumptions inherent in EB beam theory. Using EB beam theory, two different finite element models were created in MATLAB in order to compare with the experiment. These two models were referred to as the constant second area moment of inertia (constant I_y) and the variable second area moment of inertia (variable I_y) models. In the constant I_y model, the area moment of inertia was assumed to be constant for each element in the model. In the variable I_y model, the taper of the beam was accounted of via integration of I_y inside the stiffness matrix integral (Eq. 24). These two beam models were important to understand the geometric stiffness effects of the beam.

In both MATLAB codes, the value for Young's Modulus was assumed to be constant for each element in the beam. The calculation of the Young's Modulus for both beam models incorporates a constant area moment of inertia in its calculation. Thus, the only difference between the two models is the calculation of the area moment of inertia. This Young's Modulus was found to vary over the length of the beam because of geometrical and manufacturing methods. As discussed in Chapter 1.3, the layup of the rod was important to understand in this work. From the butt of the rod to the tip, the unidirectional fibers became misaligned due to the wrapping of the fibers around the tapered mandrel. Considering the unidirectional (longitudinal) direction, the layering of prepreg over the length of the tapered beam would introduce a twist to the longitudinal direction that would not align with the center axis. Thus, the Young's Modulus would have components from both the longitudinal and transverse modulus of the prepreg material due to the changing direction of the prepreg.

In the specimen used, the wall thickness of the rod was found to be consistent over the length of the beam because of the wedge shaped "flag" of prepreg material (Figure 3). These "flags" of material were measured and cut so there was a consistent amount of material around the mandrel. This can also be seen via the slope of the inside and outside rod diameters being parallel as shown in Figure 18. However, for some rod parts, the wall thickness might not be constant over the length of the rod. The finite element model created in MATLAB accounts for varying wall thickness in the beam.

In addition to these approximations, it is important to note that Euler-Bernoulli beam theory in this application uses 1D beam elements in two dimensions to represent a 3D rod. The beam model used stepped sections consisting of an isotropic Young's Modulus for the beam, and a constant mass for each element in the rod.

During the assembly of the local stiffness matrices used in the calculation, the rod was broken up into discrete elements. Each element of the rod will have its own geometric and material properties. This allows for control in the number of elements used in the MATLAB finite element model.

2.2 Euler-Bernoulli beam theory

2.2.1 Stiffness Matrix

Axial stress σ_{xx} normal to the cross-section is related to the axial strain ϵ_{xx} through Young's Modulus E [10].

$$\sigma_{xx} = E\epsilon_{xx} \tag{1}$$

Moment M around the y-axis is defined as

$$M_y(x) = \int_A z\sigma_{xx}\, dA \tag{2}$$

Where $\sigma_{xx}dA$ is the force normal to the infinitesimally small surface area dA and z is the moment arm measured from the y-axis.

$$M_y(x) = \int_A zE\epsilon_{xx}\, dA = \int_A zE\left(z\frac{\partial\theta_y}{\partial x}\right)dA = z\frac{\partial\theta_y}{\partial x}E\int_A z^2\, dA \tag{3}$$

To which is found the moment curvature relation

$$M_y(x) = EI_y\frac{\partial\theta_y}{\partial x} \tag{4}$$

Where

$$I_y = \int_A z^2\, dA \tag{5}$$

is the second area moment of inertia.

$$\sigma_y = -\frac{\partial w}{\partial x} \tag{6}$$

Then

$$M_y(x) = EI_y\frac{\partial^2 w}{\partial x^2} \tag{7}$$

$$\hat{\varepsilon} = \frac{\partial^2 w}{\partial x^2} \tag{8}$$

Infinitesimal Strain Energy is

$$\delta U = \int_{x=0}^{x=L} EI_y \, \hat{\varepsilon}\delta\hat{\varepsilon}dx \tag{9}$$

$$N_1 = 1 - 3s^2 + 2s^3, \quad N_2 = -s + 2s^2 - s^3, \tag{10}$$

$$N_3 = 3s^2 - 2s^3, \qquad N_4 = s^2 - s^3$$

Through manipulation of the assumed displacement, and incorporating the shape functions in Eq. 10 corresponding to the displacement w and rotation θ

$$w = [N_1 \;\; LN_2 \;\; N_3 \;\; LN_4] \begin{Bmatrix} w_1 \\ \theta_1 \\ w_2 \\ \theta_2 \end{Bmatrix} \tag{11}$$

The strain energy increment for element "e" is expressed as:

$$\delta U_e = \int_{x=0}^{x=L_e} EI_y \, \delta\hat{\varepsilon}\hat{\varepsilon}dx \tag{12}$$

Noting that the assumed displacement is expressed with s as a non-dimensional coordinate:

$$\hat{\varepsilon} = \frac{\partial^2 w}{\partial x^2} = \frac{\partial}{\partial s}\left(\frac{\partial w}{\partial s}\frac{\partial s}{\partial x}\right)\frac{\partial s}{\partial x} = \frac{1}{l^2}\frac{\partial^2 w}{\partial x^2} \tag{13}$$

The assumed displacement with respect to Eq. 11 can be expressed as:

$$\hat{\varepsilon} = \frac{1}{l^2}\left(\frac{\partial^2 N_1}{\partial s^2}w_1 + \frac{\partial^2 N_2}{\partial s^2}L\theta_1 + \frac{\partial^2 N_3}{\partial s^2}w_2 + \frac{\partial^2 N_4}{\partial s^2}L\theta_2\right) \tag{14}$$

$$\hat{\varepsilon} = \frac{1}{L^2}[-6+12s \quad (4-6s)L \quad 6-12s \quad (2-6s)L]\begin{Bmatrix} w_1 \\ \theta_1 \\ w_2 \\ \theta_2 \end{Bmatrix} \tag{15}$$

Symbolically:

$$\hat{\varepsilon} = \frac{1}{L^2}\boldsymbol{Bd} \tag{16}$$

Using this relation into Eq. 12:

$$\delta U_e = \frac{1}{L^4}\int_{s=0}^{s=1} EI_y\,\delta\boldsymbol{d^T B^T B d}L ds = \delta\boldsymbol{d^T}\left(\frac{1}{L^3}\int_{s=0}^{s=1} EI_y\,\boldsymbol{B^T B}ds\right)\boldsymbol{d} = \delta\boldsymbol{d^T k^e d} \tag{17}$$

Where:

$$\boldsymbol{k^e} = \frac{1}{L^3}\int_{s=0}^{s=1} EI_y\,\boldsymbol{B^T B}ds \tag{18}$$

The equation above is used in the calculation of the local stiffness matrix for the tapered area moment of inertia. With the second area moment of inertia inside the integral along with the $\boldsymbol{B}$ matrices, this is integrated in s-space over the length of the desired beam element in order to gain the local stiffness matrix for that element.

$$\boldsymbol{k}^e = \frac{2EI_y}{L^3}\begin{bmatrix} 6 & -3L & -6 & -3L \\ -3L & 2L^2 & 3L & L^2 \\ -6 & 3L & 6 & 3L \\ -3L & L^2 & 3L & 2L^2 \end{bmatrix} \tag{19}$$

With a constant second area moment of inertia, the local stiffness matrix is calculated as shown above.

Considering the equilibrium equation $KU = F$

$$\frac{2EI_y}{L^3}\begin{bmatrix} 6 & -3L & -6 & -3L \\ -3L & 2L^2 & 3L & L^2 \\ -6 & 3L & 6 & 3L \\ -3L & L^2 & 3L & 2L^2 \end{bmatrix}\begin{Bmatrix} w_1 \\ \theta_1 \\ w_2 \\ \theta_2 \end{Bmatrix} = \begin{Bmatrix} F_1^e \\ M_{y1}^e \\ F_2^e \\ M_{y2}^e \end{Bmatrix} \tag{20}$$

Integrating second area moment of inertia:

Classically, the second area moment of inertia for a hollow cylinder is given as:

$$I_y(s) = \left(\frac{\pi}{64}\right)(d_o^4(s) - d_i^4(s)) \tag{21}$$

Which was used in the constant I_y beam model. But considering the tapered section [10], let

$$d_o(s) = \frac{(d_t - d_b)}{L}s + d_b \tag{22}$$

And

$$d_i(s) = \frac{(d_t - d_b) + 2(t_b + t_t)}{L}s + d_b - 2t_b \tag{23}$$

Where the integral with respect to s is performed and d_b and d_t are the diameter at the butt and tip of each section and t_b and t_t are the wall thickness at the butt and tip of each section, respectively. By substituting Eq. 22 and Eq. 23 into Eq. 21 and then Eq. 21 into Eq. 18, it can be

determined that the closed-form of the Euler-Bernoulli stiffness matrix given the thin-walled hollow tapered cylinder is found to be

$$\boldsymbol{k}^e = \frac{E}{L^3}\int_{s=0}^{s=L}\left(\left(\frac{\pi}{64}\right)\left(\left(\frac{(d_t-d_b)}{L}s+d_b\right)^4-\left(\frac{(d_t-d_b)+2(t_b+t_t)}{L}s+d_b-2t_b\right)^4\right)\right)\boldsymbol{B}^{\boldsymbol{T}}\boldsymbol{B}ds \tag{24}$$

After integrating Eq. 24, the matrix form of the Euler-Bernoulli beam theory for a thin-walled hollow tapered cylinder was be found to be

$$\left(\frac{35E\pi}{512L^2}\right)\begin{bmatrix}K_{11} & K_{12} & K_{13} & K_{14}\\ K_{21} & K_{22} & K_{23} & K_{24}\\ K_{31} & K_{32} & K_{33} & K_{34}\\ K_{41} & K_{42} & K_{43} & K_{44}\end{bmatrix}\begin{Bmatrix}w_1\\ \theta_1\\ w_2\\ \theta_2\end{Bmatrix}=\begin{Bmatrix}F_1^e\\ M_{y1}^e\\ F_2^e\\ M_{y2}^e\end{Bmatrix} \tag{25}$$

Where:

$$\begin{aligned}
K_{11} = (&132d_b^3t_b + 15d_b^3t_t + 45d_b^2d_t t_b + 18d_b^2d_t t_t - 396d_b^2t_b - 90d_b^2t_b t_t - 18d_b^2t_t^2 + 18d_b d_t^2 t_b\\
&+ 45d_b d_t^2 t_t - 90d_b d_t t_b^2 - 72d_b d_t t_b t_t - 90d_b d_t t_t^2 + 528d_b t_b^3 + 180d_b t_b^2 t_t\\
&+ 72d_b t_b t_t^2 + 60d_b t_t^3 + 15d_t^3 t_b + 132d_t^3 t_t - 18d_t^2 t_b^2 - 90d_t^2 t_b t_t - 396d_t^2 t_t^2\\
&+ 60d_t t_b^3 + 72d_t t_b^2 t_t + 180d_t t_b t_t^2 + 528d_t t_t^3 - 264t_b^3 - 120t_b^3 t_t - 72t_b^2 t_t^2\\
&- 120t_b t_t^3 - 264t_t^4)/L^2\\
K_{12} = -(&94d_b^3t_b + 11d_b^3t_t + 33d_b^2d_t t_b + 9d_b^2d_t t_t - 282d_b^2t_b^2 - 66d_b^2t_b t_t - 9d_b^2t_t^2 + 9d_b d_t^2 t_t\\
&+ 12d_b d_t^2 t_t - 66d_b d_t t_b^2 - 36d_b d_t t_b t_t - 24d_b d_t t_t^2 + 376d_b t_b^3 + 132d_b t_b^2 t_t\\
&+ 36d_b t_b t_t^2 + 16d_b t_t^3 + 4d_t^3 t_b + 38d_t^3 t_t - 9d_t^2 t_b^2 - 24d_t^2 t_b t_t - 114d_t^2 t_t^2 + 44d_t t_b^3\\
&+ 36d_t t_b^2 t_t + 48d_t t_b t_t^2 + 152d_t t_t^3 - 188t_b^4 - 88t_b^3 t_t - 36d_b^2 t_t^2 - 32t_b t_t^3 - 76t_t^4)/L\\
K_{13} = &-K_{11}\\
K_{14} = -(&38d_b^3t_b + 4d_b^3t_t + 12d_b^2d_t t_b + 9d_b^2d_t t_t - 114d_b^2t_b^2 - 24d_b^2t_b t_t - 9d_b^2t_t^2 + 9d_b d_t t_b\\
&+ 33d_b d_t^2 t_t - 24d_b d_t t_b^2 - 36d_b d_t t_b t_t - 66d_b d_t t_t^2 + 152d_b t_b^3 + 48d_b t_b^2\\
&+ 36d_b t_b^2 t_t^2 + 44t_b t_t^3 + 11d_t^3 t_b + 94d_t^3 t_t - 9d_t^2 t_b^2 - 66d_t^2 t_b t_t - 282d_t^2 t_t^2 + 16d_t t_t^3\\
&+ 36d_b t_b^2 t_t + 132d_t t_b t_t^2 + 376d_t t_t^3 - 76t_b^4 - 32t_b^3 t_t - 36t_b^2 t_t^2 - 88t_b t_t^3\\
&- 188t_t^4)/L\\
K_{21} = &K_{12}
\end{aligned}$$

$$K_{22} = (68d_b^3t_b + 9d_b^3t_t + 27d_b^2d_tt_b + 8d_b^2d_tt_t - 204d_b^2t_b^2 - 54d_b^2t_bt_t - 8d_b^2t_t^2 + 8d_bd_t^2t_b + 6d_bd_t^2t_t$$
$$- 54d_bd_tt_b^2 - 32d_bd_tt_bt_t - 12d_bd_tt_t^2 + 272d_bt_b^3 + 108d_bt_b^2t_t + 32d_bt_bt_t^2 + 8d_bt_t^3$$
$$+ 2d_t^3t_b + 12d_t^3t_t - 8d_t^2t_b^2 - 12d_t^2t_bt_t - 36d_t^2t_t^2 + 36d_tt_b^3 + 32d_tt_b^2t_t + 24d_tt_bt_t^2$$
$$+ 48d_tt_t^3 - 136t_b^4 - 72t_b^3t_t - 32t_b^2t_t^2 - 16t_bt_t^3 - 24t_t^4)$$

$$K_{23} = -K_{12}$$

$$K_{24} = (26d_b^3t_b + 2d_b^3t_t + 6d_b^2d_tt_b + d_b^2d_tt_t - 78d_b^2t_b^2 - 12d_b^2t_bt_t + d_b^2t_t^2 + d_bd_t^2t_b + 6d_bd_t^2t_t$$
$$- 12d_bd_tt_b^2 - 4d_bd_tt_bt_t - 12d_bd_tt_t^2 + 104d_bt_b^3 + 24d_bt_b^2t_t + 4d_bt_bt_t^2 + 8d_bt_t^3$$
$$+ 2d_t^3t_b + 26d_t^3t_t - d_t^2t_b^2 - 12d_t^2t_bt_t - 78d_t^2t_t^2 + 8d_tt_b^3 + 4d_tt_b^2t_t + 24d_tt_bt_t$$
$$+ 104d_tt_t^3 - 52t_b^4 - 16t_b^3t_t - 4t_b^2t_t^2 - 16t_bt_t^3 - 52t_t^4)$$

$$K_{31} = -K_{11}$$

$$K_{32} = -K_{12}$$

$$K_{33} = K_{11}$$

$$K_{34} = -K_{14}$$

$$K_{41} = K_{14}$$

$$K_{42} = K_{24}$$

$$K_{43} = -K_{14}$$

$$K_{44} = (12d_b^3t_b + 2d_b^3t_t + 6d_b^2d_tt_b + 8d_b^2d_tt_t - 36d_b^2t_b^2 - 12d_b^2t_bt_t - 8d_b^2t_t + 8d_bd_t^2t_b + 27d_bd_t^2t_t$$
$$- 12d_bd_tt_b^2 - 32d_bd_tt_bt_t - 54d_bd_tt_t^2 + 48d_bt_b^3 + 24d_bt_b^2t_t + 32d_bt_bt_t^2 + 36d_bt_t^3$$
$$+ 9d_t^3t_b + 68d_t^3t_t - 8d_t^2t_b^2 - 54d_t^2t_bt_t - 204d_t^2t_t^2 + 8d_tt_b^3 + 32d_tt_b^2t_t + 108d_tt_bt_t^2$$
$$+ 272d_tt_t^3 - 24t_b^4 - 16t_b^3t_t - 32t_b^2t_t^2 - 72t_bt_t^3 - 136t_t^4)$$

2.2.2 Unit Test Verification

Unit tests were conducted to confirm the results from Eq. 20 and Eq. 25 are consistent. The results of solving Eq. 20 and Eq. 25 were compared with results from the MATLAB codes. The unit tests were performed using a two element simply supported beam with a cantilever point load.

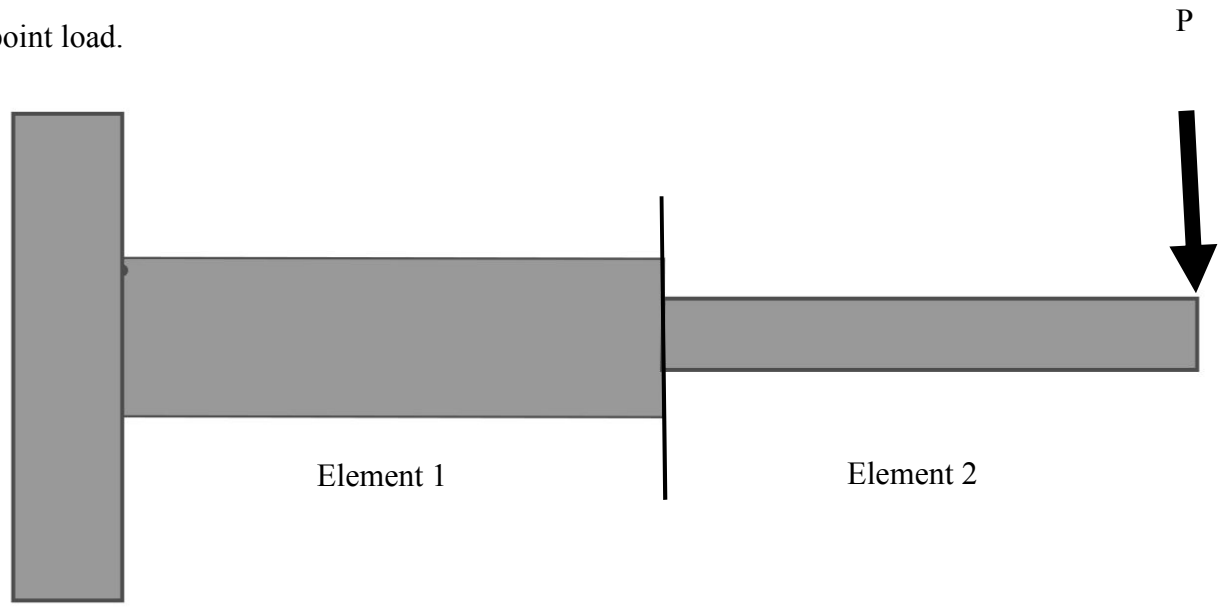

Figure 7 - Constant I_y beam model verification

First, the constant I_y case is considered (Figure 7). Constant values of E, I_y, and L were implemented using Eq. 20. These constant values were given to be E =1, I_1 = 4, I_2=3, and L = 10. The boundary conditions at node one were $w_1 = 0$ and $\theta_1 = 0$ with a point load $P = -1$ applied at the end of the beam (F_2^2). After inverting the stiffness matrix and solving for w_2 and w_3, the values were found to be:

Unit Test	Displacement w_2	Displacement w_3
Hand calculation	-208.3333	-694.4444
MATLAB code	-208.3333	-694.4444

Table 1 - Constant I_y unit test results

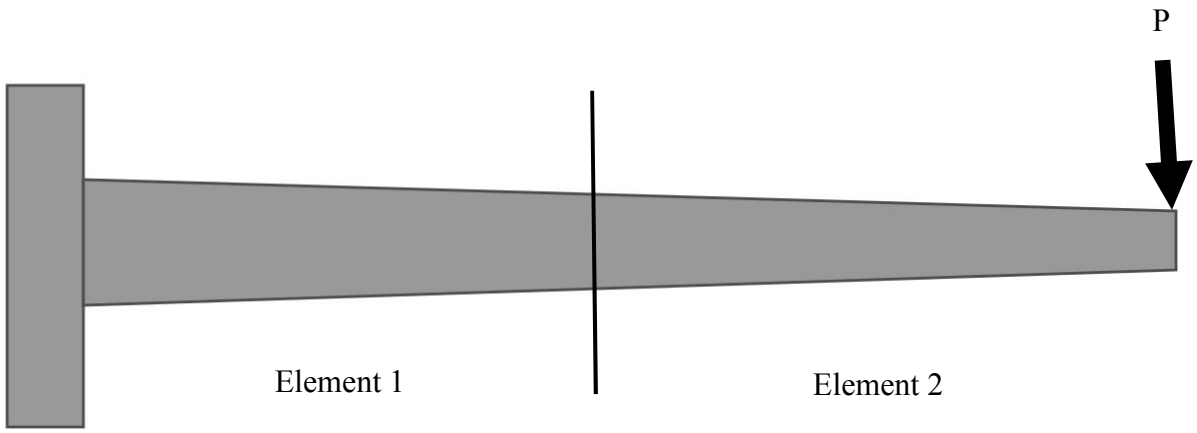

Figure 8 - Variable I_y beam model verification

A second unit test verification was performed considering variable I_y using Eq. 25 (Figure 8). A two element simply supported beam with a cantilever point load is also used for the test. More constant values are needed in this approach. For the two-element model,

Value	Element 1	Element 2
d_b	20	15
d_t	15	10
t_b	2	0.5
t_t	1	1
L	100	100
E	1	1

Table 2 - Variable I_y unit test values

These values were used in the variable I_y model for both the hand calculations and the MATLAB code. The boundary conditions at node one were the same as the constant I_y case, but the point load P was given to be -0.00001. The results of the unit test are seen below.

Unit Test	Displacement w_2	Displacement w_3
Hand calculation	-0.000136988	-0.000682857
MATLAB code	-0.000136988	-0.000682857

Table 3 - Variable I_y unit test results

These unit tests verify that the application of boundary conditions, solving of stiffness matrices, and assembly of local stiffness matrices are consistent between the MATLAB code and a simple hand calculation. A refinement study was completed using dimensions of the test specimen rod subject to cantilever boundary conditions. The constant I_y converges to the variable I_y model as the number of elements increases (Figure 9).

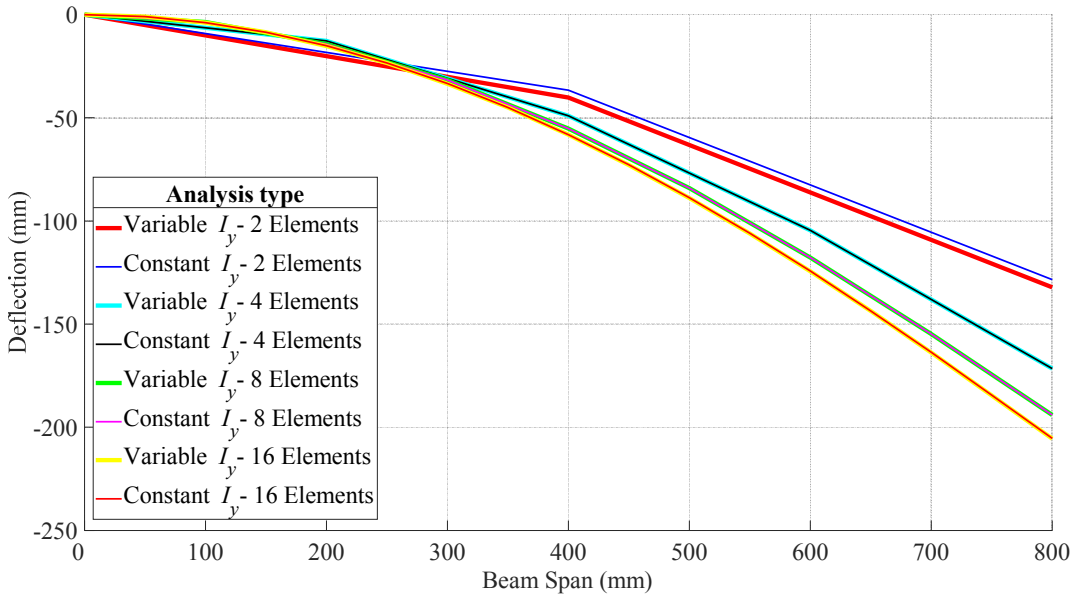

Figure 9- Convergence study with refinement

2.2.3 Mass Matrix and Modal Analysis

A calculation of the beam modes will also be beneficial in the analysis of rods [9] [10] [11].

$$\delta W = \int_{x=0}^{x=L} \delta w p_z dx + (P_L \delta w)_{x=L} \tag{26}$$

Shown above is the incremental work δW for an applied cantilever loading condition, neglecting the effect of cross-sectional rotation. $p_z(x,t)$ is the applied force per unit length. $P_L(t)$ is the force applied at $x = L$. $w(x,t)$ is the transverse displacement. With the inertial force as an applied force per unit length, for the segment of length dx:

$$p_z dx = -(m dx)\ddot{w} \tag{27}$$

Where m is the mass per unit length. For the entire body:

$$-\int_{x=0}^{x=L} \delta w p_z dx = \int_{x=0}^{x=L} \delta w \ddot{w} m dx \tag{28}$$

For a two-node bending element,

$$w = \boldsymbol{N}\boldsymbol{d}, \qquad w = \boldsymbol{N}\ddot{\boldsymbol{d}}, \qquad \delta w = \boldsymbol{N}\delta\boldsymbol{d} = \delta\boldsymbol{d}^{\boldsymbol{T}}\boldsymbol{N}^{\boldsymbol{T}} \tag{29}$$

Where

$$N = [N_1 \;\; N_2 l \;\; N_3 \;\; N_4 l] \tag{30}$$

with the shape functions being.

(31)

$$N_1 = 1 - 3s^2 + 2s^3, \quad N_2 = -s + 2s^2 - s^3,$$

$$N_3 = 3s^2 - 2s^3, \qquad N_4 = s^2 - s^3$$

and

$$\boldsymbol{d} = \begin{Bmatrix} w_1 \\ \theta_1 \\ w_2 \\ \theta_2 \end{Bmatrix}\text{: element DOF vector} \tag{32}$$

Accordingly:

$$-\int_{x=x_1}^{x=x_2} \delta w p_z dx = \int_{x=x_1}^{x=x_2} \delta w \ddot{w} m dx = \int_{s=0}^{s=1} \delta \boldsymbol{d}^T \boldsymbol{N}^T \boldsymbol{N} \ddot{\boldsymbol{d}} m l ds \tag{33}$$

$$= \delta \boldsymbol{d}^T \left(l \int_{s=0}^{s=1} \boldsymbol{N}^T \boldsymbol{N} m ds \right) \ddot{\boldsymbol{d}} = \delta \boldsymbol{d}^T \boldsymbol{m}^e \ddot{\boldsymbol{d}} \tag{34}$$

Where

$$\boldsymbol{m}^e = l \int_{s=0}^{s=1} \boldsymbol{N}^T \boldsymbol{N} m ds \tag{35}$$

Is the element mass matrix, and for a constant m it can be shown that:

$$\boldsymbol{m}^e = \frac{ml}{420} \begin{bmatrix} 156 & -22 & 54 & 13 \\ -22 & 4 & -13 & -3 \\ 54 & -13 & 156 & 22 \\ 13 & -3 & 22 & 4 \end{bmatrix} \tag{36}$$

However, in this model a constant m over the length of the whole rod is not applicable, because the mass of the rod changes with the taper, wall section, and material density of the length of the rod. A linear regression was performed with respect to the mass density of the material and the volume of the material for each cut section of the rod. This allows for the fully integrated mass matrix to be used in the calculation of the mode shapes, using Eq. 34.

Now the equation of motion of the entire structure of the beam can be shown as:

$$-\int_{x=x_1}^{x=x_2} \delta w p_z dx = \int_{x=x_1}^{x=x_2} \delta w \ddot{w} m dx = \delta \boldsymbol{q}^T \boldsymbol{M} \ddot{\boldsymbol{q}} \tag{37}$$

Where $\boldsymbol{M}$ is the global mass matrix and $\ddot{\boldsymbol{q}}$ is the global acceleration vector.

This can be constructed into the equation of motion of the beam, combined with the beam stiffness as:

$$\boldsymbol{M}\ddot{\boldsymbol{q}} + \boldsymbol{K}\boldsymbol{q} = \boldsymbol{F} \tag{38}$$

To solve for free vibration of the cantilever beam (F=0), where $\boldsymbol{q}$ is an $N \times 1$ DOF vector. With the reduced form after geometric boundary conditions are applied, Eq. 38 is homogeneous and produces a solution of the following form.

$$\boldsymbol{q} = \boldsymbol{\varphi} e^{pt} = \boldsymbol{q} = \boldsymbol{\varphi} e^{\pm i\omega t} \tag{39}$$

For an oscillatory response with no energy loss (no damping).

$$(\boldsymbol{K} - \omega^2 \boldsymbol{M})\boldsymbol{\varphi} e^{\pm i\omega t} = 0 \tag{40}$$

Since $e^{\pm i\omega t} \neq 0$ for all time t:

$$(\boldsymbol{K} - \omega^2 \boldsymbol{M})\boldsymbol{\varphi} = 0 \tag{41}$$

For nontrivial $\boldsymbol{\varphi}$, Eq. 41 can be solved in an eigenfunction analysis, with "det" being the determinant.

$$det(\boldsymbol{K} - \omega^2 \boldsymbol{M})\boldsymbol{\varphi} = 0 \tag{42}$$

With ω^2 eigenvalues with N dof, there are N eigenvalues counting multiple roots. $\boldsymbol{\varphi}$ is the eigenvector corresponding to ω. For a standard eigenvalue analysis:

$$\boldsymbol{K}\boldsymbol{\varphi} = \lambda \boldsymbol{M}\boldsymbol{\varphi} \tag{43}$$

Where:

$$\lambda = \omega^2 \tag{44}$$

For the *i*th mode

$$\boldsymbol{K\varphi}_i = \lambda_i \boldsymbol{M\varphi}_i \;\rightarrow\; \boldsymbol{K\varphi}_i = \omega_i^2 \boldsymbol{M\varphi}_i \tag{45}$$

For a system with *N* DOF, there are *N* natural frequencies and *N* natural modes, counting multiple roots separately. ω_i are arranged in increasing order of magnitude, starting with ω_1 as the lowest frequency.

2.3 Specimen Manufacturing

For the specimens used in the following analysis, Thomas and Thomas Fly Rod Company, located in Greenfield, Massachusetts provided eight test parts. These parts were made with a prepreg incorporating Mitsubishi HR40 carbon fiber. After an entire four-piece fly rod is assembled, it will consist of a tip, tip-mid, butt-mid, and butt section (Figure 10). The taper and construction of this test part corresponds to the tip-mid section of a saltwater fly-fishing rod.

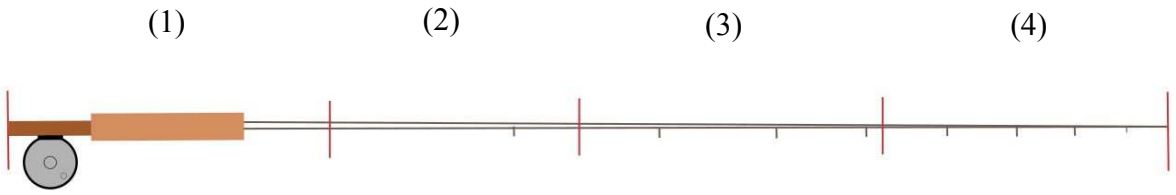

Figure 10 - Rod pieces Butt (1), Butt-Mid (2), Tip-Mid (3), Tip (4)

Dimensions of parts. Test parts were 800mm long, with the largest outer diameter (OD) at the bottom of the part (butt) and smallest OD at the tip. Given the length of the part, some rods were

cut in a bandsaw for use in 3PB (3-point bending) tests. These parts were cut into 100mm sections, resulting in a total of 8 parts for the 3PB test (Figure 11).

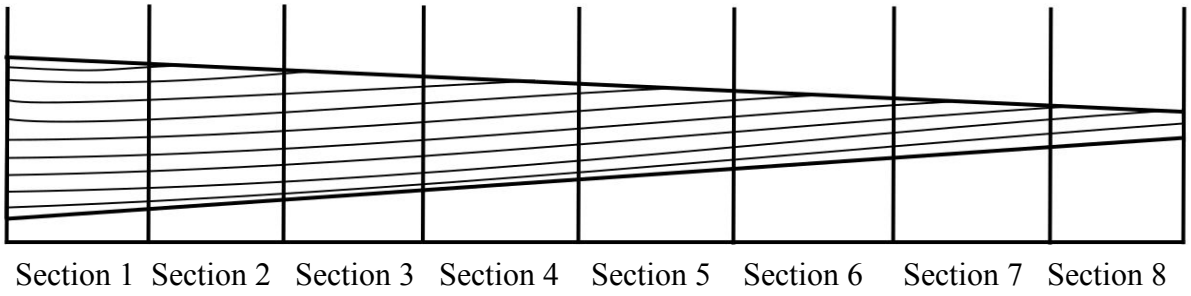

Figure 11 – Rod Sections

2.4 Experimental procedure: Young's Modulus

A value of Young's Modulus (E) was needed for the numerical procedure in this ICME approach. Using a Tinius Olsen H25kt universal testing machine located in GEDMIL at the University of Maryland located in the Kim engineering building, the value was determined from a 3PB test, ASTM D790. For this test, the 800mm test part was cut into eight 100mm sections. Each one of these sections corresponds to an element in the Euler-Bernoulli beam theory used in MATLAB. These sections were placed into a 3PB test jig. The span of the two rollers supporting the rod is 90mm. This left a 5mm overhang over each end of the section to reduce free-end boundary effects. The point load was applied directly at the center of the rod as shown in Figure 12 and Figure 13. Data was collected at all stages of the test. The data given during the test was the deflection at the center of test part (mm), and the force applied (N). This data was then analyzed for linearity. In a 3PB test, depending on the material, a non-linear regime can be achieved, due to the non-linear effects of material behavior during the loading process.

The Euler-Bernoulli beam theory only holds for the linear effects of a material, so the data needed to be analyzed in order to determine when this non-linearity occurs. In Excel, the data was plotted for each test section. In the early stages of the test, the linear properties of the material can be seen. A low force and deflection were determined to be stable in the linear regime of the test.

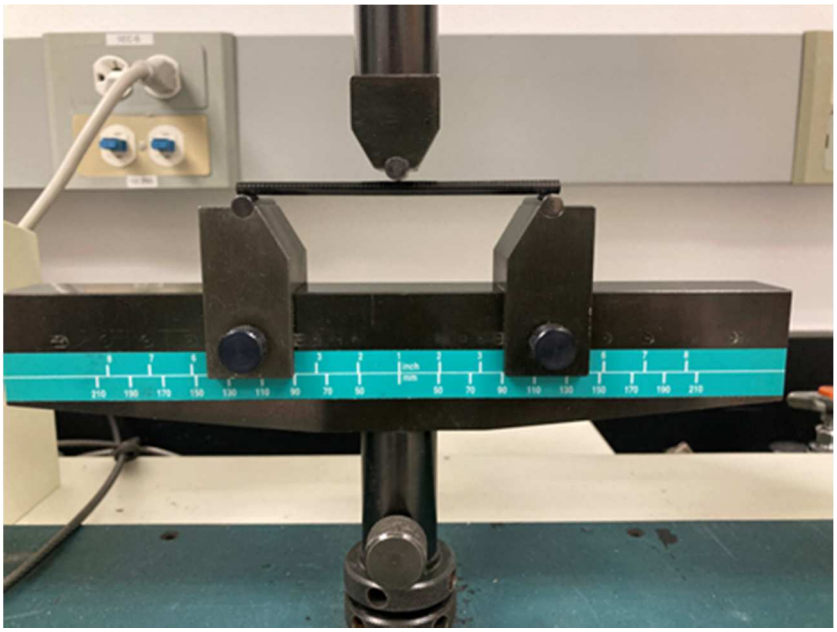

Figure 12 – Unloaded 3PB

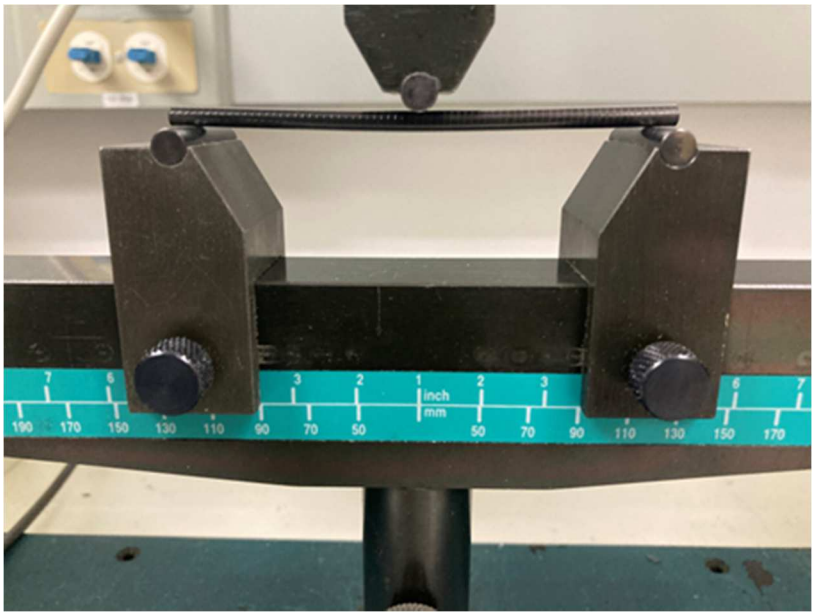

Figure 13 – Loaded 3PB

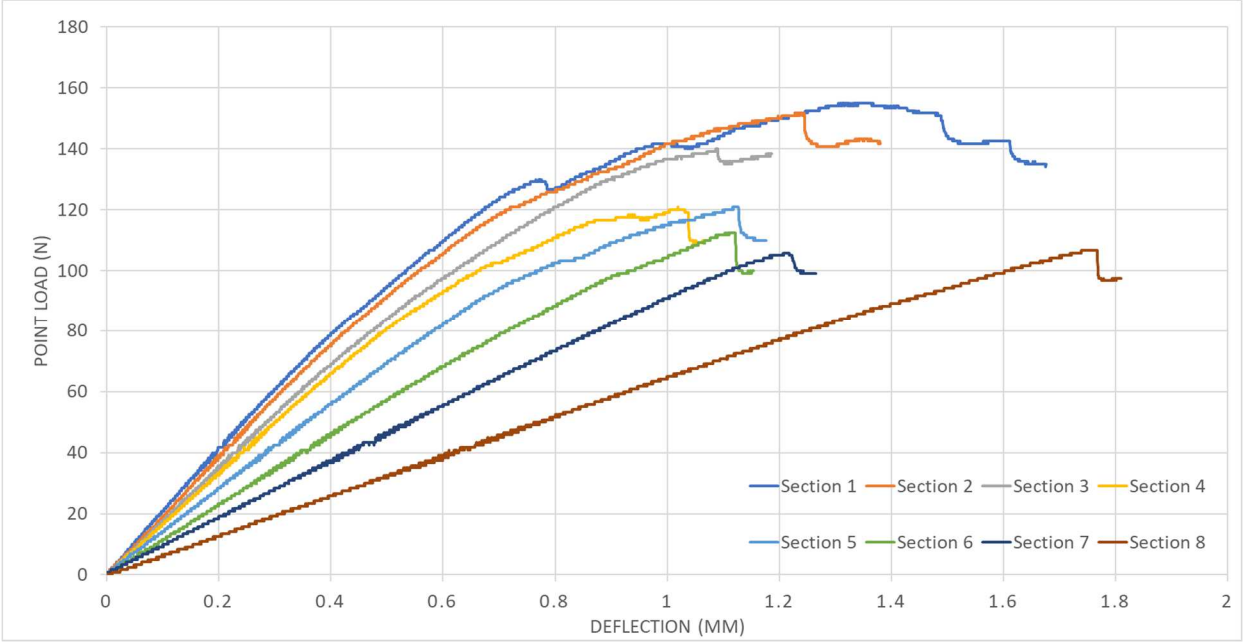

Figure 14 – 3PB Force Deflection Experimental Results

Figure 14 shows the results from the 3PB analysis performed on the beam sections. The sections were loaded until a yield was detected. This yield was determined by observing the force-deflection curves during loading and looking for a drop in force during the loading, or by audio-visual cues such as cracking or visual deformation in the material of the test specimen.

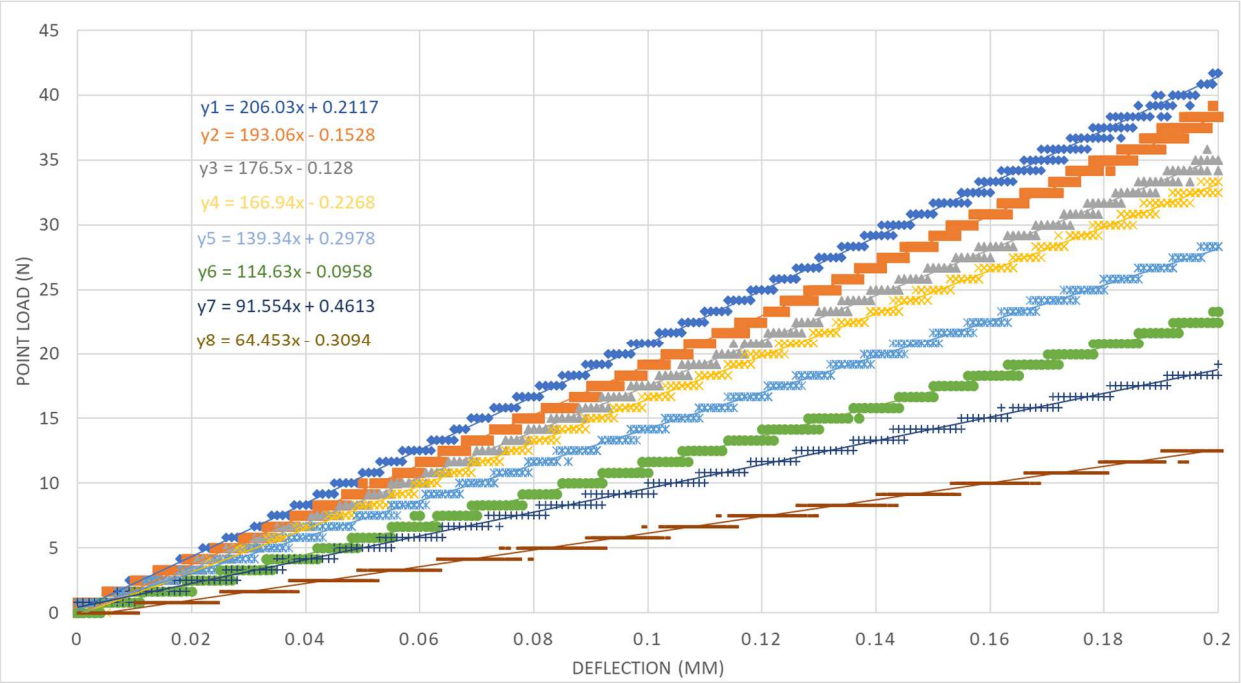

Figure 15 – 3PB Force Deflection Experimental Results (Linear Regime)

A linear regression was performed on linear regime of the experimental results, shown in Figure 15. These equations were then solved for the force at a given deflection, in this case 0.1mm (Figure 16).

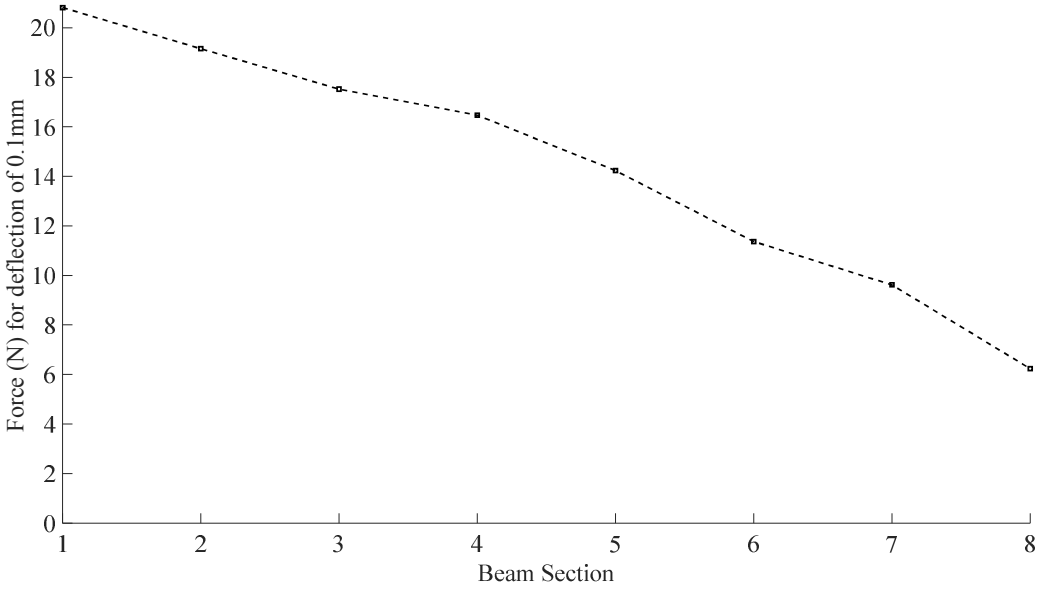

Figure 16 – Force for deflection of 0.1mm during 3PB test for each beam section

A linear regression of Figure 16 was used to determine the force required for a 0.1mm deflection of the beam during the experimental procedure for determining Young's Modulus. After the maximum force and central vertical displacement values for each part were determined, a simple manipulation of the deflection at the center of a three-point flexure test equation for beam bending is used to determine E [12] [13].

$$E = \frac{WL^3}{48I\delta} \tag{46}$$

This E in Eq. 46 is then used in the MATLAB analysis. Shown in Figure 17, the Young's Modulus was found to increase over the length of the beam.

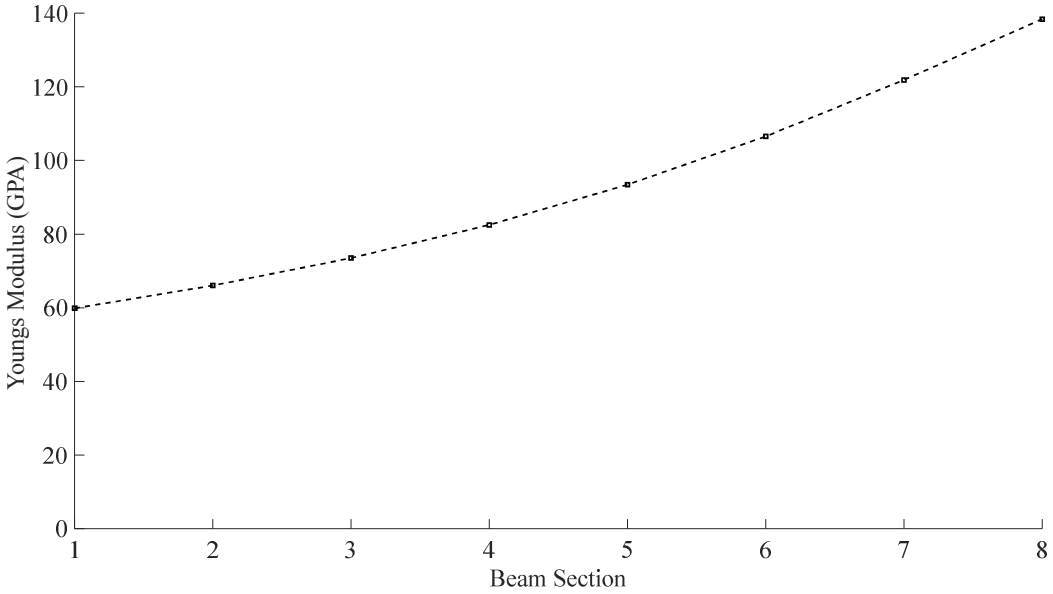

Figure 17 – Young's Modulus E for each beam section.

The inside and outside diameters of the beam were found to be linear. This was because of the linearly tapered mandrel used during manufacturing along with the uniform wall thickness. A plot of the diameters is shown below in Figure 18 and this allowed for a linear regression to be made for discretization in the code to determine the second area moment of inertia, I_y.

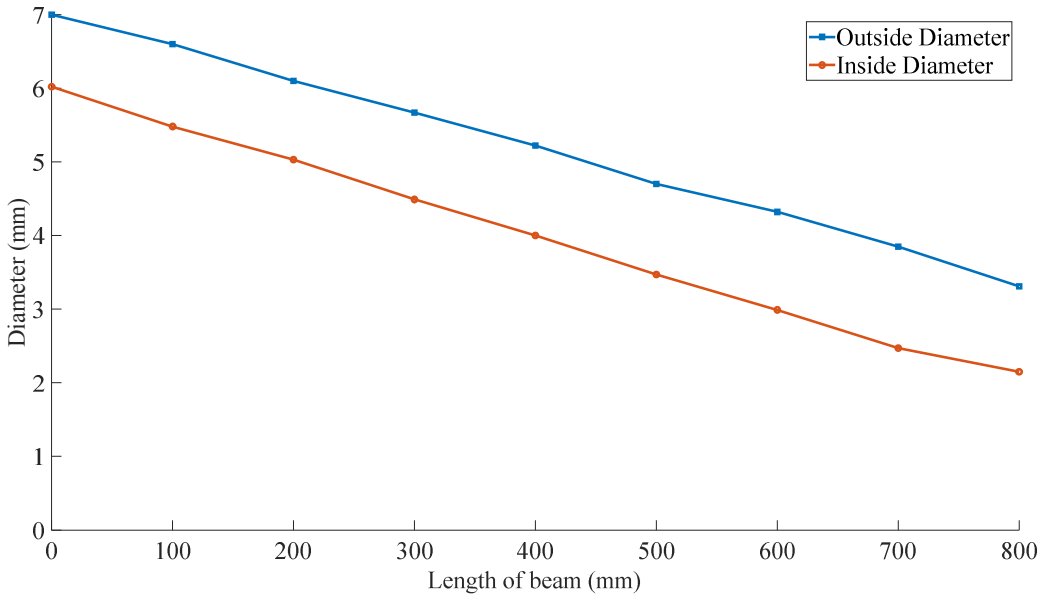

Figure 18 – Inside and outside diameters of the beam with measurements taken at 100mm intervals.

2.5 Numerical Analysis and Justification

Using the Euler – Bernoulli beam theory derived above, a MATLAB finite element code was constructed to create a robust way to model deflections on the test parts. This allows for a simplification of the entire rod to a discretized element length. The code allows the user to set the number of elements to see the effects of mesh size given the boundary conditions and load. The local stiffness and mass matrices were assembled into global matrices.

Two different boundary and loading conditions were performed on each model. A cantilever boundary condition of fixed displacement and rotation with a 5N cantilevered point load was is performed.

A second boundary condition was also used in order to gain values to compare the experiment to the numerical solution. A 3PB test was used to determine the bending of the rod

with a 5N point load at the center of a beam span. The roller support span on the 800mm long rod was 600mm, in order to reduce free end boundary effects [14].

As mentioned in the theory above, two different uses of Euler-Bernoulli beam theory were performed to model the beam. A variable I_y (Eq. 24) over each beam element model using the shape functions to determine local stiffness matrices along with a constant I_y over each element beam model (Eq. 20) were created in MATLAB. The variable I_y considers the changing area moment of inertia. The variable I_y was found to be almost equal to the constant I_y (Figure 19).

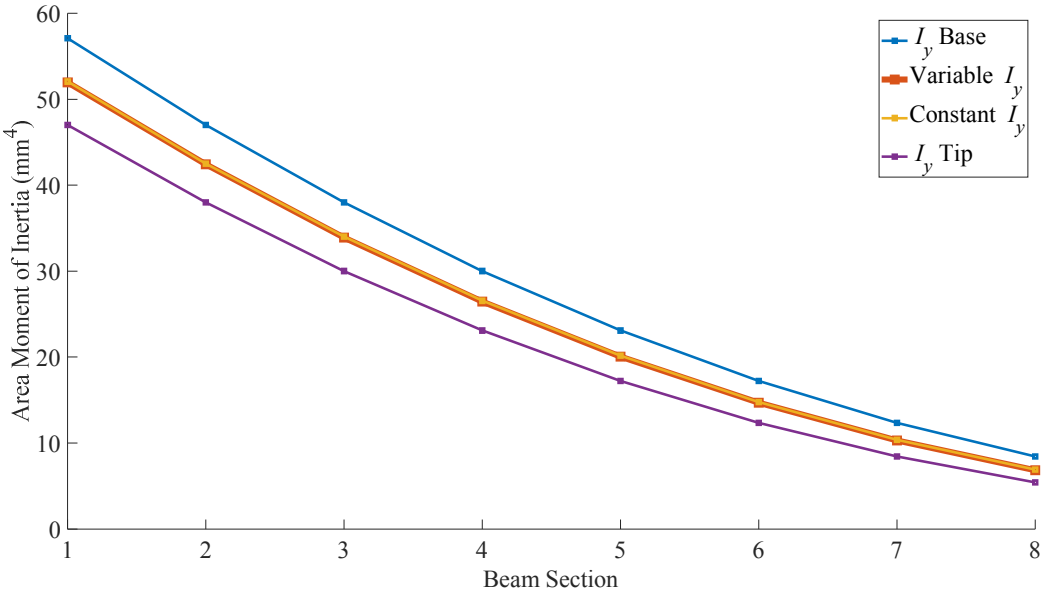

Figure 19 – I_y over the length of the beam

In the MATLAB code, the boundary conditions are applied after assembly. The code for displacement analysis accounts for the location of the boundary condition location automatically with respect to the number of elements used. In addition to the deflection analysis, a modal analysis of the beam was also performed. The boundary conditions for the modal analysis consisted of an unconstrained free vibration and a cantilevered free vibration condition.

A test rod specimen was loaded in a 3PB test (Figure 20) using the 3PB bending condition described above. IC Measure software with a stable zoom camera was used to determine the deflection at eleven points corresponding to deflection measurements over the course of the length of the beam.

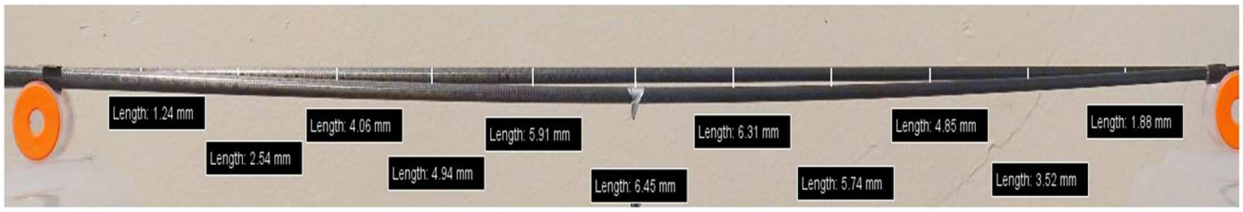

Figure 20 – 3PB Experiment

2.6 Steel 3PB Experiment

The experiment and numerical solution were validated with a test of a 3.175mm diameter plain steel rod with a Young's Modulus of 200GPa. The theoretical equation used to determine the Young's Modulus in Eq. 46 was found to match the corresponding finite element model created in MATLAB. The experiment yielded a maximum deflection of 22.62mm (Figure 21). In the finite element model, the maximum deflection at the center of the steel rod with a 5N load was found to be 22.5532mm (Figure 22).

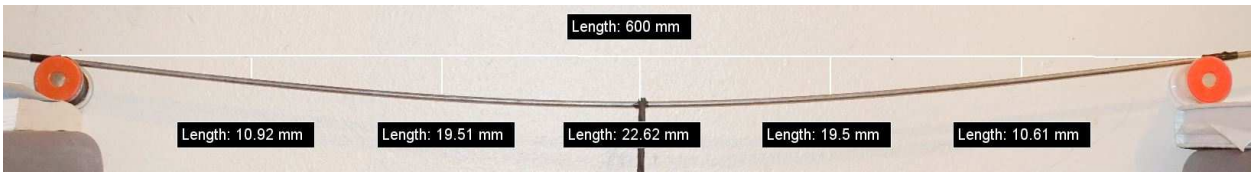

Figure 21 – Steel 3PB flexure test – experiment

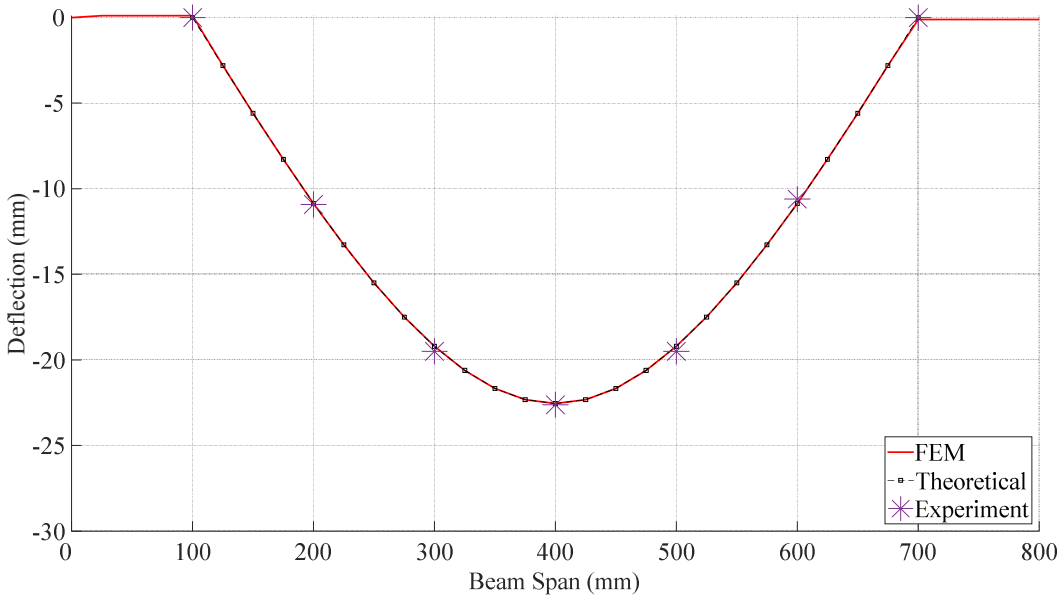

Figure 22 – Steel 3PB flexure test – 32 element model

Chapter 3 : Results and Discussion

3.1 Three-point bending condition

Shown in Figure 23-25 are results of the 3PB flexure experiment plotted with the constant I_y and variable I_y beams. The variable I_y and constant I_y beam show correlation with the experiment at a low element count and show good deflection characteristics compared to the experiment as the number of elements increases.

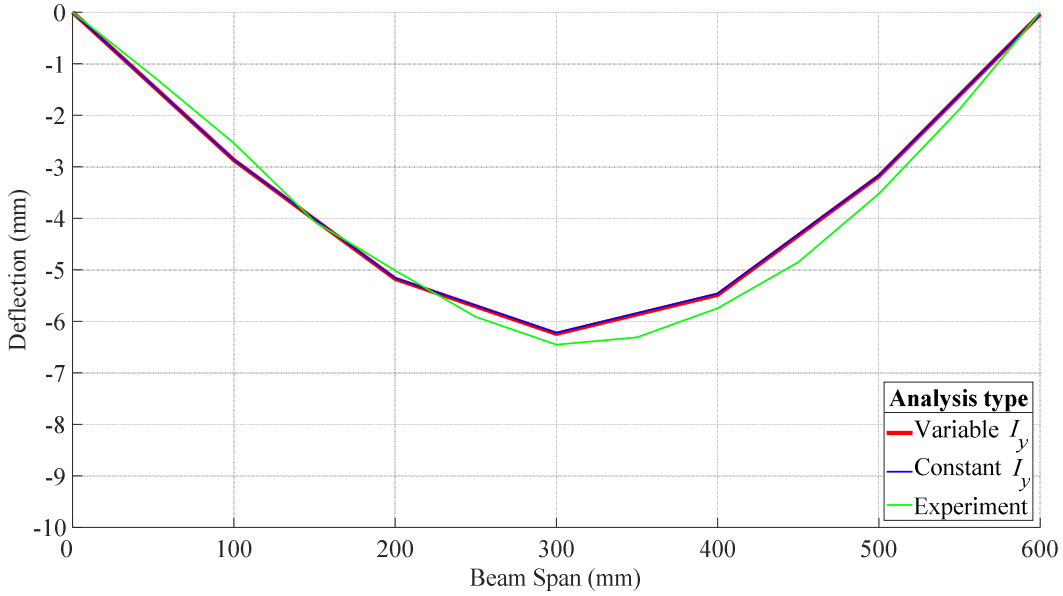

Figure 23 – 3PB Results – 8 Elements

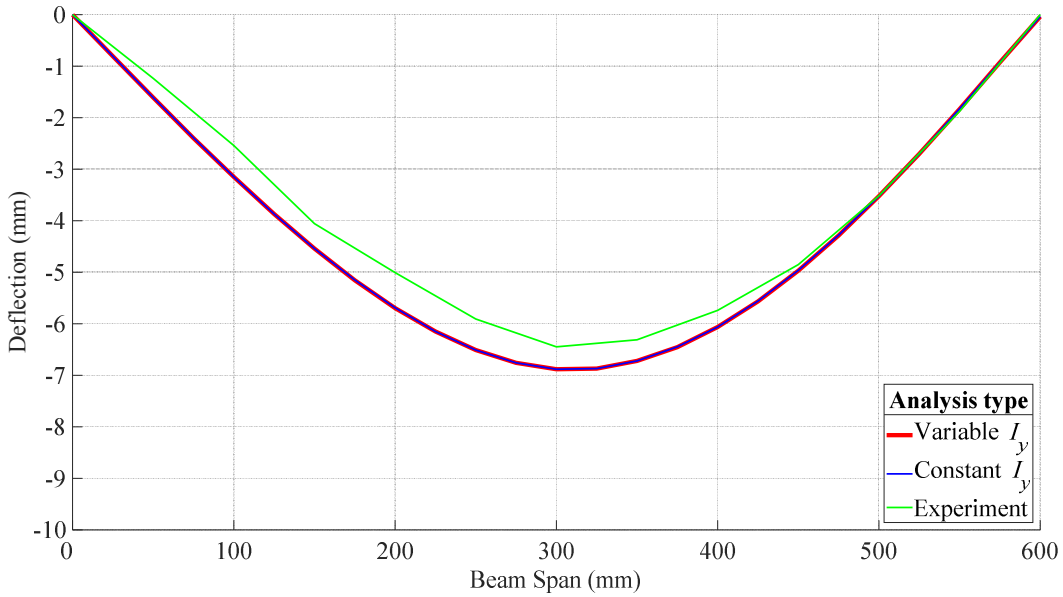

Figure 24 – 3PB Results – 32 Elements

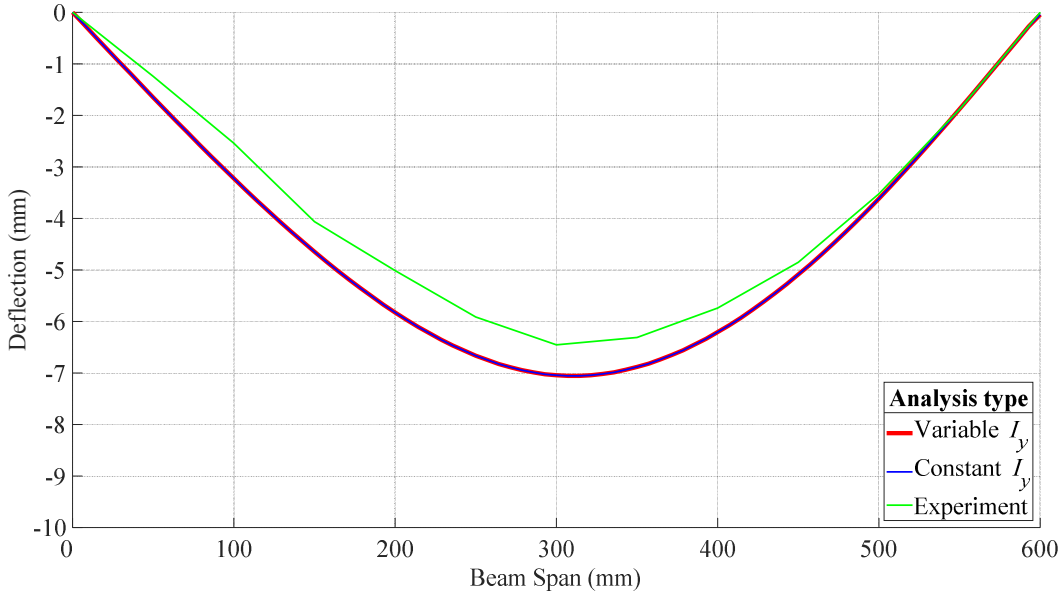

Figure 25 – 3PB Results – 112 Elements

At 112 elements, the constant I_y and variable I_y beam deflections show very good agreement (Figure 25).

3.2 Cantilever bending condition

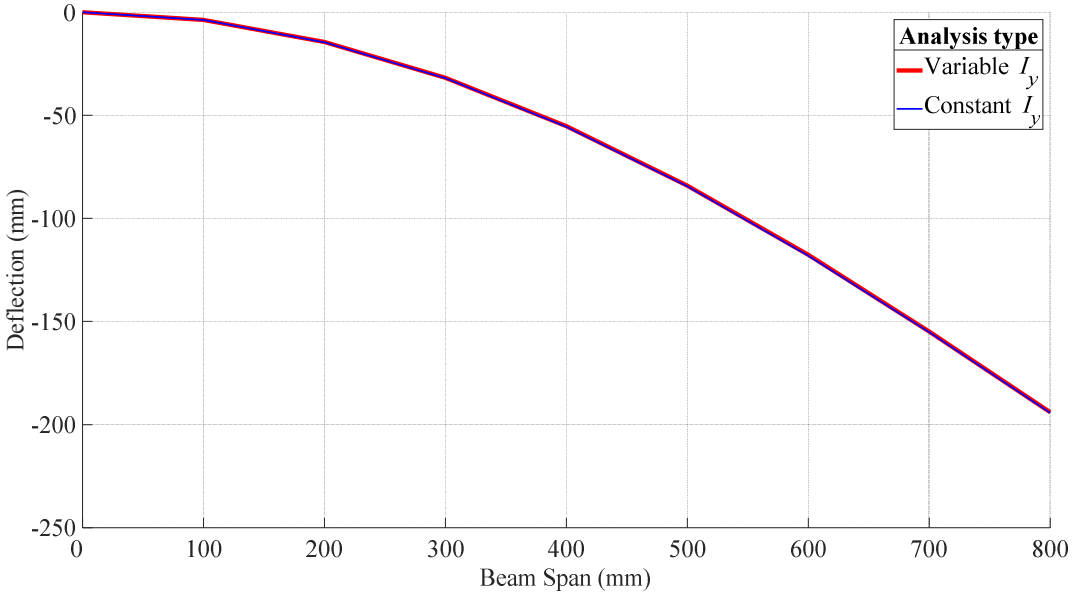

Figure 26 – Cantilever bending condition – 8 Elements

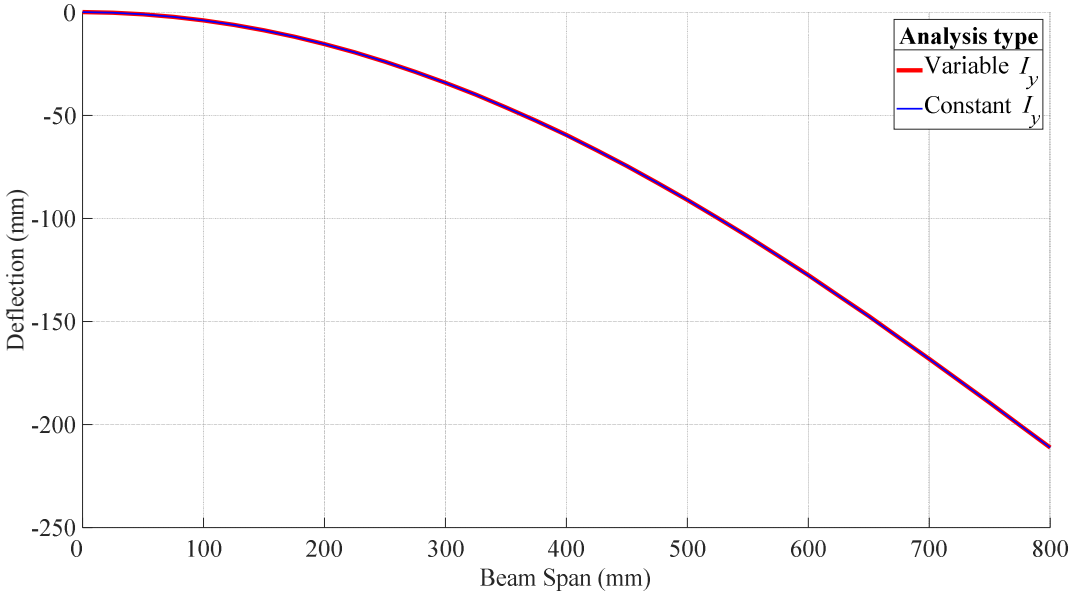

Figure 27 – Cantilever bending condition – 32 Elements

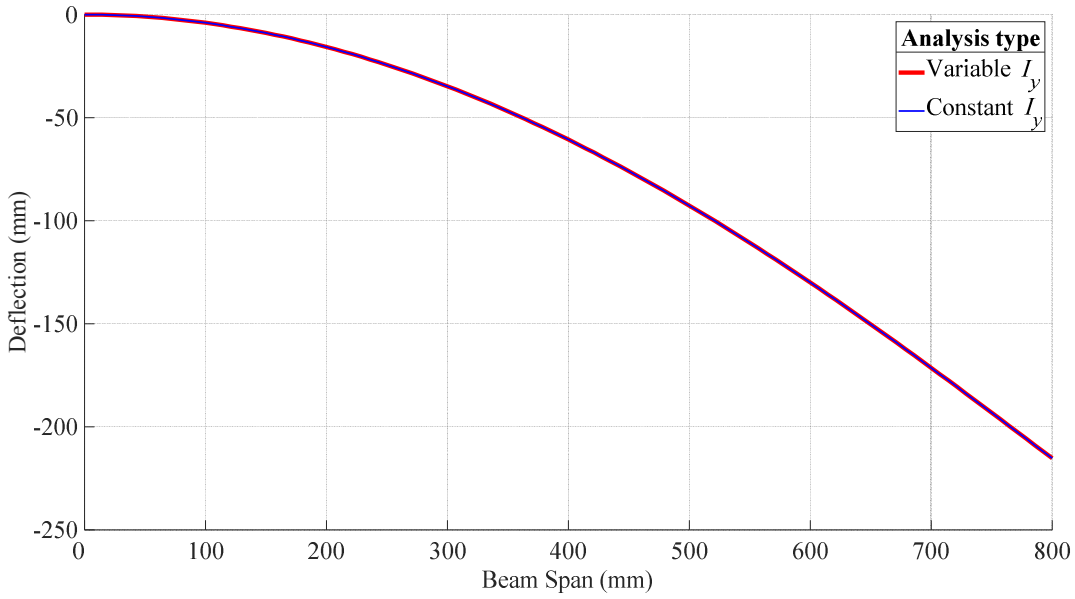

Figure 28 – Cantilever bending condition – 112 Elements

Shown above are the results of the cantilever loading conditions applied to the constant I_y and variable I_y beams (Figures 26-28)

3.3 Modal Analysis results

The modal analysis can provide insight to how the rod will perform once the rod is unloaded during a cast. Normalized eigenvectors were found and plotted for a free vibration of the beam with and without a cantilever boundary condition applied. A 112-element beam was normalized, and the relevant modes were studied. The modes plotted are the most important to this beam analysis. They represent the lowest frequencies that the rod would experience. When a user of the rod has a rigid grip on the handle, the rod will experience modes like the cantilever boundary condition (Figure 30). If a user relaxes their grip on the rod, the free vibrational modes will be like the mode shapes shown without boundary conditions (Figure 29). Both boundary conditions are important to understand the complete picture of how a rod will rebound and resonate during and after a cast.

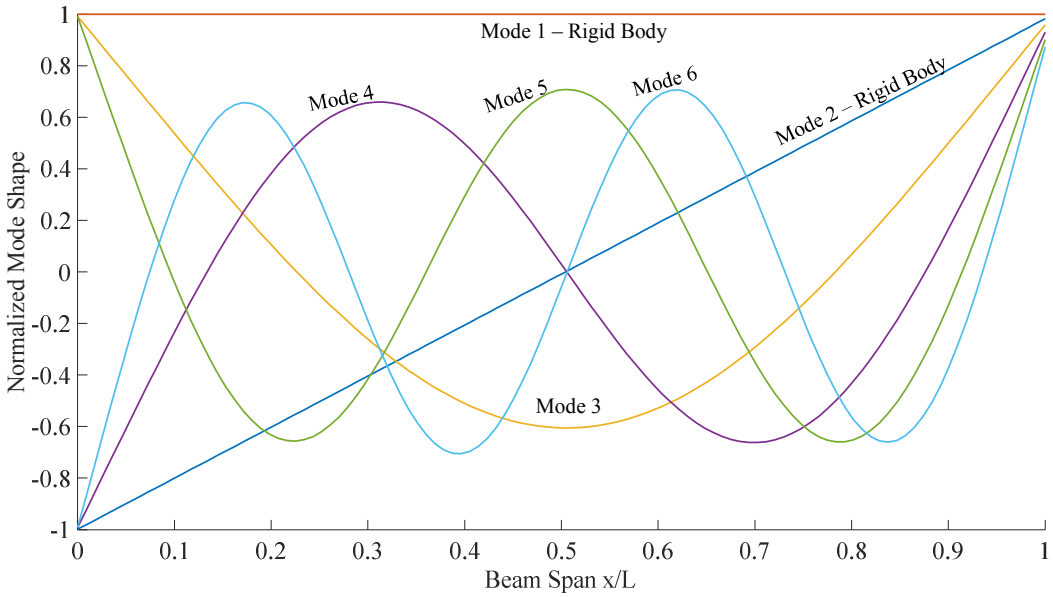

Figure 29 – Mode Shapes without boundary conditions

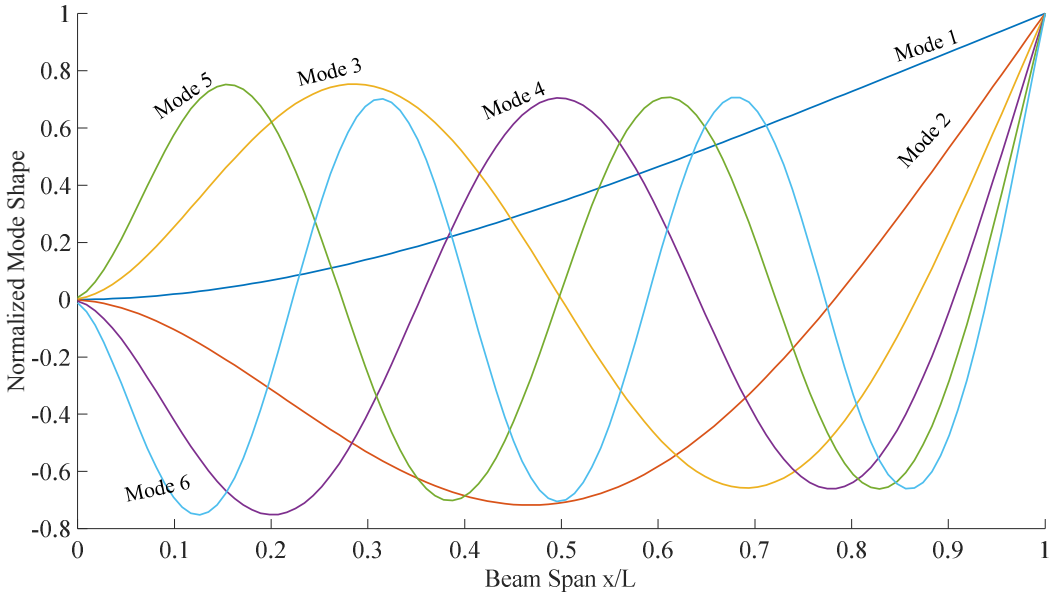

Figure 30 – Mode Shapes with Cantilever Boundary Condition

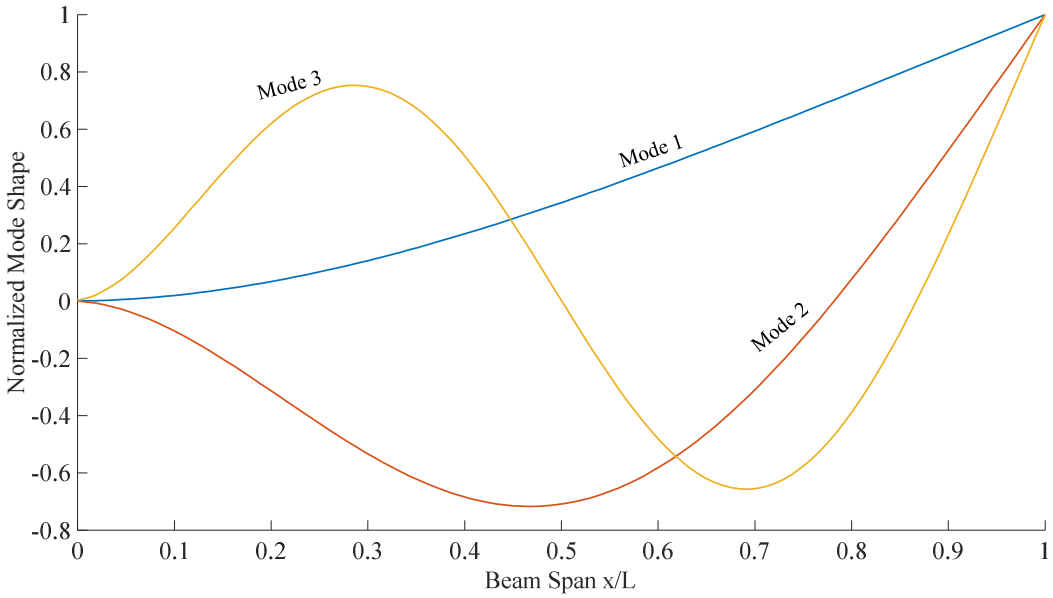

Figure 31 – First Three Mode Shapes with Cantilever Boundary Condition

3.4 Discussion of results

Results of the 3-point flexure loading condition show good adherence to the experiment (Figure 25). As the number of elements increases, the variable I_y beam converges to the constant I_y beam. Via a least mean-square convergence test (Figure 32), this can be shown as the error between the constant I_y and variable I_y beam decreases as mesh size increases.

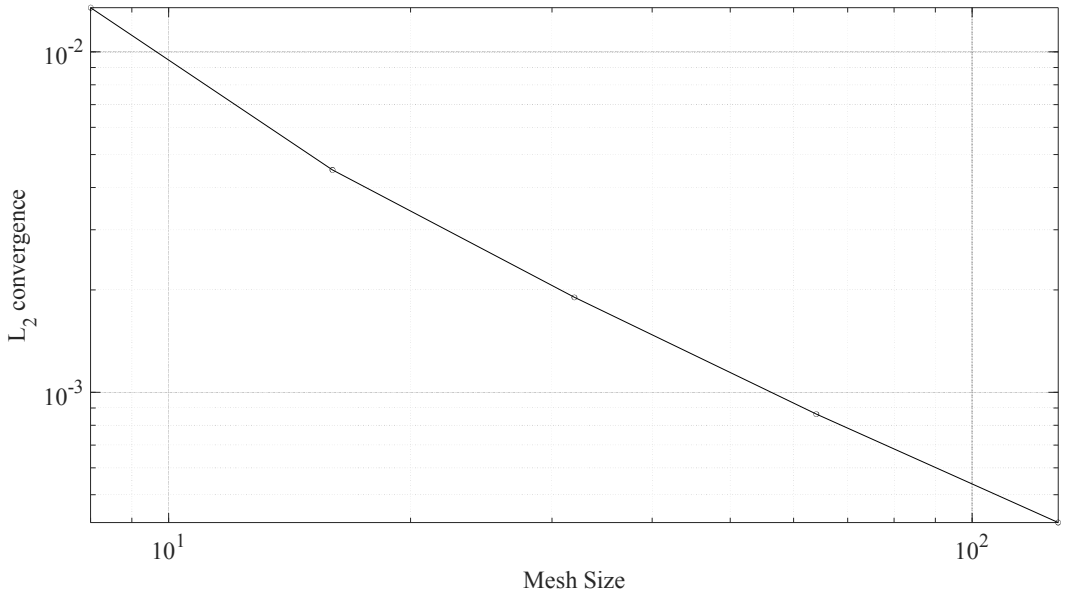

Figure 32 – Least mean-square Convergence with respect to mesh size for the constant I_y beam to variable I_y beam.

At 112 elements, the constant I_y and variable I_y beam models show good agreement with the 3PB experiment. As shown in Figure 19, the values for constant I_y and variable I_y are almost exact over the length of the beam. The refinement study (Figure 9) shows that at a low number of elements the FE models start to converge as the elements become smaller. This results in excellent agreement between the constant I_y and variable I_y numerical solutions.

The modal analysis provides insight into the mode shapes the rod experiences during free vibration. The two boundary conditions studied cover the boundary conditions that fishermen would experience during use of a rod. When a user relaxes their grip on the rod, the modes the rod experiences would be like modes three and four shown in the analysis without boundary conditions. When the user has a tighter grip on the rod, such as during a cast, the modes of the rod change.

The first three modes shown in the modal analysis with a cantilever boundary condition considered provide insight into how the rod would resonate during the casting stroke (Figure 31) [2]. The knowledge of the modes experienced comes from personal experience using fly-fishing rods.

Chapter 4: Conclusion

4.1 Main Contributions

The results of the deflection analysis and modal analysis give insight to the properties of rod design. By modifying the taper profile and materials used, these analysis techniques can be used to designed new tapers and rods. A consistent bending profile is very important to the design of a rod. With many differences in weights and lengths of rods, having a robust numerical model to describe the bending of a new rod design will reduce research and development time and allow for expedient prototyping. Key takeaways from this thesis include:

- The 3PB solution shows justification for testing individual sections to determine the Young's Modulus.
- The constant I_y section beam model converges to the variable I_y beam model.
- The difference between the variable I_y model and constant I_y model is minimal. Constant I_y models could be used in the future for further analysis. This can be seen in Figure 16 and the results in Chapter 3.
- Complex layups can be used in this model, with differing these prepreg layups accounted for by the experimentally found Young's Modulus.
- The relationship between the Young's Modulus and the area moment of inertia is crucial to analysis. This means the relationship between material, taper profile and wall thickness is one of the most important factors in rod design.

4.2 Design

Designing new rods can be aided by this approach. The four parameters that dictate rod design are the mandrel taper, wall thickness of the hollow cross section, material choice, and overall mass of the rod. A material suited for one mandrel taper and wall thickness may give the desired bending characteristics, but at the cost of increased mass. Wall thickness, mandrel taper, and material can then be chosen in a way that reduces mass but gives the desired stiffness. The method of quantifying and predicting the bending characteristics of thin-walled tapered hollow carbon fiber rods outlined in this thesis provides valuable information for the design of fishing rods.

The modal analysis serves as an exercise into how vibrational analysis can be conducted on fly rods. The taper and material used effect these vibrational modes. Rod designers can use this information to see how different tapers and materials effect these vibrational modes.

4.3 Future Work

The non-linear effects of the cantilever beam are important for modelling the rod. Rod designers currently use deflection curves (Figure 6) as a crucial component during the prototyping and design phase for new rod models. Further study into the effects of large deformation should be considered in future work. Non-linear large deformation Euler-Bernoulli beam theory has proven to be accurate to experimental results [8]. Combined with the ICME method of analysis for determining the Young's Modulus through experimental testing, this would allow for the analysis of large deflection loads applied to complex rod designs.

As discussed in Chapter 2, the use of Euler-Bernoulli beam theory introduces critical assumptions and limitations into the model. 1D beam elements with two degrees of freedom do not allow for cross sectional deformation or distortion. When a rod is loaded, the cross section

will deform and not retain its circular shape. In recent years, rod manufacturers are using new layup methods to account for this deformation and simultaneously increase hoop strength [16].

3D models of the rod would prove very valuable in rod design. The use of 3D shell elements in programs such as ANSYS would allow rod designers to conduct stress and large deformation analysis. These models will also account for cross-sectional deformation.

Further study into the modal analysis with added damping could also be conducted. By introducing damping into the rod, mode shapes of the rod that would negatively affect casting performance could be analyzed and accounted for in design. Adding small dampers inside the rod could provide enhanced resonance control to the rod or change the mode shapes to help with a smoother casting stroke and better rod recovery after a cast.

This thesis studies one section of a current saltwater fly rod. Studying a full-length fly-fishing rod should be considered in future analysis as this will provide valuable information for rod design. The methods of analysis used in this thesis can easily be scaled for use in the study of a full-length fly rod.

Overall, this thesis provides the basis for a ICME approach to the study of thin-walled carbon rods with complex carbon fiber prepreg layups. Through the numerical approach of Euler – Bernoulli beam theory, current rods and the rods of the future can be better understood and designed.

Bibliography

[1] "Bamboo Fly Rods History," Willow and Cane, [Online]. Available: http://www.willowandcane.com/history-of-split-bamboo-fly-rods.html. [Accessed 16 December 2021].

[2] "Understanding Fly Rod Balance, Swing Weight, Deflection, Continuity and Frequency," Mac Brown Fly Fish, 7 January 2018. [Online]. Available: https://macbrownflyfish.com/fly-rod-attributes/understanding-fly-rod-balance-swing-weight-deflection-continuity-frequency/. [Accessed 15 December 2021].

[3] "Technology," Scott Fly Rods, [Online]. Available: https://www.scottflyrod.com/technology. [Accessed 23 May 2022].

[4] "How Fly Rods Are Made," Midcurrent, [Online]. Available: https://midcurrent.com/gear/how-fly-rods-are-made. [Accessed 2 June 2022].

[5] "How To Choose A Fly Rod - A Buyer's Guide," Angling Active, 30 July 2018. [Online]. Available: https://www.anglingactive.co.uk/blog/choosing-a-fly-rod-buyers-guide/. [Accessed 29 May 2022].

[6] "Deflection Charts - 2019 4-Weight Shootout," Yellowstone Angler, 2 July 2019. [Online]. Available: https://www.yellowstoneangler.com/gear-review/2019-4-weight-shootout/deflection-charts-2019-4-weight-shootout/. [Accessed 28 May 2022].

[7] M. e. al., "Numerical-experimental approach to assess the deflection behaviour of carbon fibre fishing rod," *IOP Conference Series: Materials Science and Engineering,* p. 012065, 23 06 2020.

[8] M. Silverman and J. Farrah, "Bending of a Tapered Rod: Modern Application and Experimental Test of Elastica Theory," *World Journal of Mechanics,* vol. 8, pp. 272-300, 2018.

[9] S. W. Lee and P. W. Chung, Finite element method for solids and structures: a concise approach, New York: Cambridge University Press, 2021.

[10] A. Skender, Z. Domitran and J. Krokar, "The Effective Flexural Modulus of Filament Wound GRP Tapered Poles," *Tehnicki vejesnik,* vol. 27, no. 6, pp. 1894-1903, 2020.

[11] T. J. R. Hughes, The Finite Element Method, Engelwood Cliffs: Prentice Hall, 1987.

[12] H. Y. Shang, R. D. Machado and J. E. Abdalla Filho, "Dynamic analysis of Euler–Bernoulli beam problems using the Generalized Finite Element Method," *Computers & Structures,* vol. 173, pp. 109-122, 2016.

[13] F. Mujika, "On the effect of shear and local deformation in three-point bending tests," *Polymer Testing,* vol. 26, no. 7, pp. 869-877, 2007.

[14] R. Eberle, "A new method for estimating the bending stiffness curve of non-uniform Euler-Bernoulli beams using static deflection data," *Applied Mathematical Modelling,* vol. 105, pp. 514-533, 2022.

[15] M. Wesolowski, B. Evgeny, S. Ručevskis, A. Chate and G. Delfa, "Characterisation of elastic properties of laminated composites by non-destructive techniques," 2009.

[16] "R8 Technology," Farbank Enterprises , 2022. [Online]. Available: https://farbank.com/pages/sage-r8-technology. [Accessed 25 July 2022].